

Article

Petrogenesis of Shihuiyao Rare-Metal Granites in the Southern Great Xing'an Range, NE China

Deyou Sun ¹, Shicheng Wang ¹, Jun Gou ^{1,*}, Duo Zhang ¹, Changzhou Deng ², Dongguang Yang ³ and Li Tian ⁴

¹ College of Earth Sciences, Jilin University, Changchun 130061, China; sundy@jlu.edu.cn (D.S.); wangshicheng243@163.com (S.W.); zhangduo20@mails.jlu.edu.cn (D.Z.)

² State Key Laboratory of Ore Deposit Geochemistry, Institute of Geochemistry, Chinese Academy of Sciences, Guiyang 550081, China; changzhouhn@126.com

³ Radioactive Geology and Exploration Technology Laboratory, East China University of Technology, Nanchang 330013, China; yangdg@ecut.edu.cn

⁴ Key Laboratory of Mineral Resources Evaluation in Northeast Asia, Ministry of Natural Resources, Changchun 130061, China; tianli21@mails.jlu.edu.cn

* Correspondence: goujun@jlu.edu.cn; Tel.: +86-139-4482-5221

Abstract: Shihuiyao Rb–Nb–Ta-rich granites from the Late Jurassic period are newly discovered rare-metal-bearing granites found in the southern Great Xing'an Range, NE China. Further research of these granites may contribute to better understanding the petrogenesis of rare-metal granites and their associated mineralization mechanisms. The granites are high-silica ($\text{SiO}_2 = 73.66\text{--}77.08$ wt%), alkali-rich ($\text{K}_2\text{O} + \text{Na}_2\text{O} = 8.18\text{--}9.49$ wt%) and weakly to mildly peraluminous with A/CNK values (molar ratios of $\text{Al}_2\text{O}_3 / (\text{CaO} + \text{Na}_2\text{O} + \text{K}_2\text{O})$) ranging from 1.06 to 1.16. High differentiation indexes (DI = 95–97) and low P_2O_5 contents demonstrate that Shihuiyao rocks are low-P and peraluminous rare-metal granites. Mineral chemistry and whole-rock geochemistry can be used to obtain the following lithological sequence: zinnwaldite granite, muscovite–zinnwaldite granite, amazonite-bearing granite and amazonite pegmatite. The effect of the rare-earth element tetrad; low K/Rb (18.98–32.82), Nb/Ta (2.41–4.64) and Zr/Hf (5.99–8.80) ratios; and the occurrence of snowball-textured quartz suggest that extreme magmatic fractionation might be the key factor that causes Rb–Nb–Ta enrichment.



Citation: Sun, D.; Wang, S.; Gou, J.; Zhang, D.; Deng, C.; Yang, D.; Tian, L. Petrogenesis of Shihuiyao Rare-Metal Granites in the Southern Great Xing'an Range, NE China. *Minerals* **2023**, *13*, 701. <https://doi.org/10.3390/min13050701>

Academic Editor: Jean-Michel Lafon

Received: 6 April 2023

Revised: 16 May 2023

Accepted: 19 May 2023

Published: 21 May 2023



Copyright: © 2023 by the authors. Licensee MDPI, Basel, Switzerland. This article is an open access article distributed under the terms and conditions of the Creative Commons Attribution (CC BY) license (<https://creativecommons.org/licenses/by/4.0/>).

Keywords: rare-metal granites; Shihuiyao; Great Xing'an Range

1. Introduction

In recent years, vigorous explorations have been carried out with the aim of discovering new rare-element mineral deposits in China. Previous research in South China has proposed a linkage between highly evolved granites and rare-element mineralization (e.g., Renli Nb–Ta, Shizhuyuan W–Sn and Jiepailing Sn–Be–F deposits in Hunan Province [1–4]; Yichun Ta–Nb and Xihuashan W–Be–REE deposits in Jiangxi Province [5,6]). Highly evolved rare-metal-bearing granites are small bodies, but they are major suppliers of several “critical” rare metals (e.g., Li, Be, Rb, W, Sn, Nb, Ta). Rare-metal enrichment in highly evolved magmatic systems is controlled by their primitive magma composition and the process of magmatic differentiation or magmatic–hydrothermal transition. Highly evolved granites are fractionated residual melts that are rich in ore-bearing metals [7]. Studies of these granites may aid our understanding of the geochemical behavior of rare metals during late magmatic processes.

In the Great Xing'an Range and its adjacent areas, several rare-metal granite bodies have been identified, the most important of which are Weilasituo Sn–Li–Rb [8–11], Zhaojinggou Nb–Ta [12] and Shihuiyao Rb–Nb–Ta deposits [13]. Many studies focus on the two former deposits [8–12] and these Sn–Li–Rb–Nb–Ta orebodies are temporally and genetically related to Early Cretaceous granitoids [13]. Different from the two former deposits,

Shihuiyao rare-metal mineralization is related to Late Jurassic granitic bodies. The Ta_2O_5 and Nb_2O_5 contents in the mineralized zone of the Shihuiyao granites vary from 0.015 to 0.282 wt%. The concentrations of Rb_2O in this zone range from 0.11 to 0.233 wt% [14,15]. Although these deposits have not yet been mined or developed, the scientific study of Shihuiyao Rb–Nb–Ta deposits has increased substantially in the past three years. Petrography, mineralogy, isotope geochemistry and geochronological investigations on granites and minerals, such as columbite [16], cassiterite [17], fluorite [14] and monazite [18], have greatly improved our understanding of Rb–Nb–Ta mineralization mechanisms. Comparatively speaking, the chemical differentiation and formation of rare-metal granitic melts are relatively more complicated, and further research is needed to determine petrogenetic details. Shihuiyao granites involve various lithologies, and their evolutionary sequences are crucial for studying the petrogenesis and metallogeny of Shihuiyao intrusion. Therefore, a systematic study of major and trace element geochemistry, as well as mineral chemistry, was carried out to determine the magma source and prolonged magmatic evolution of Shihuiyao granites by synthesizing new mineralogical and geochemical data with previous findings.

2. Geology and Petrography

Shihuiyao rare-metal granite is located in the southern Great Xing'an Range within the interior of the Songnen Block (Figure 1a). The Songnen Block lies between the Hegenshan and Xar Moron sutures and predominantly comprises juvenile continental crust [19]. The ages of the Xilingol complex range from 1005 to 1026 Ma [20], likely representing a small fragment of Precambrian basement rocks. Since the Phanerozoic period, the Songnen Block has witnessed the evolution of the Paleo-Asian and Paleo-Pacific Oceans. During the Late Jurassic and Early Cretaceous periods, the subduction of the Paleo-Pacific plate led to extensive magmatic activities and a greater petrogenetic diversity of igneous rocks [21–26]. Magmatism in the Songnen Block is closely related to various kinds of polymetallic mineralization (Sn, Li, Rb, Cu, Pb, Zn, etc.).

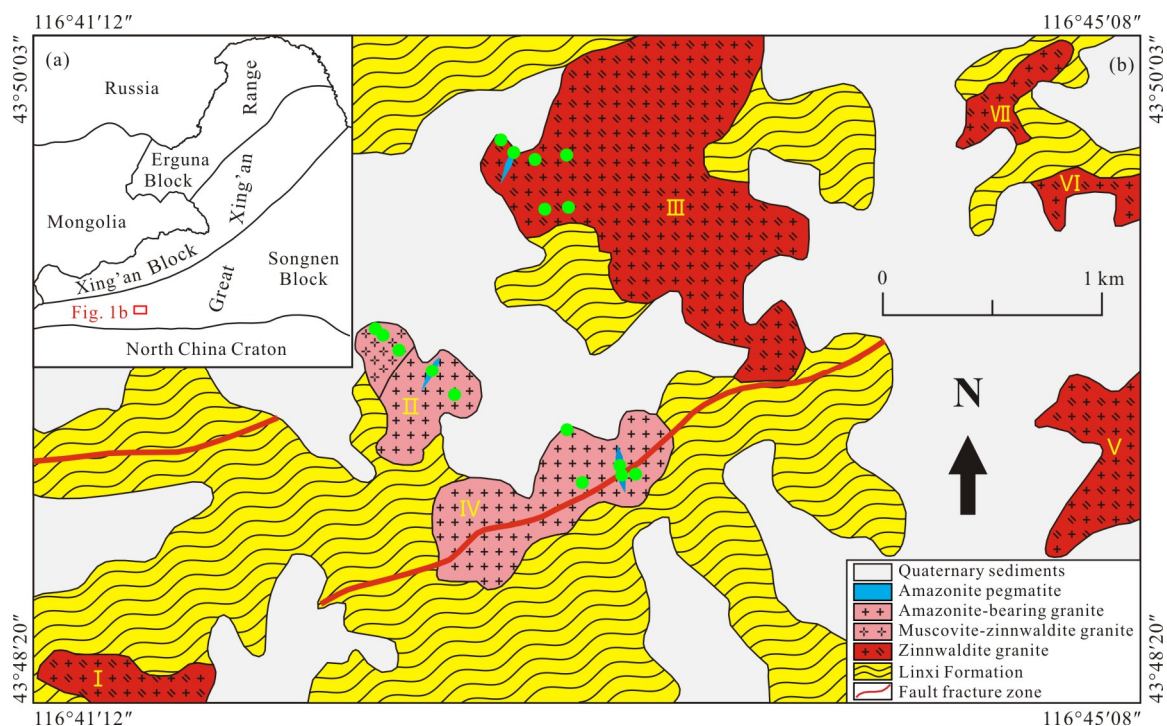


Figure 1. (a) Simplified tectonic map showing the location of the study area in NE China. (b) Distribution of Late Jurassic Shihuiyao granites (modified after [15]). The mapped stocks are numbered I–VII, and the solid green circles are sample localities.

The Shihuiyao Rb–Nb–Ta-rich granite is located 10 km northeast of Baiyinxile Town, Xilinhot City. This complex was identified in 1986 by geological survey or exploration works of the No. 109 geology survey team of Inner Mongolia Autonomous Region and had been mapped to seven small stocks numbered I–VII (Figure 1b), with the maximum exposed area (stock III) of 1.38 km² [15]. These stocks form the highest massif in terms of topography and intrude into Permian sedimentary rocks of the Linxi Formation. Shihuiyao granite consists of four distinct granitic phases, including zinnwaldite granite, muscovite–zinnwaldite granite, amazonite-bearing granite and quartz–amazonite pegmatite (Figure 2).

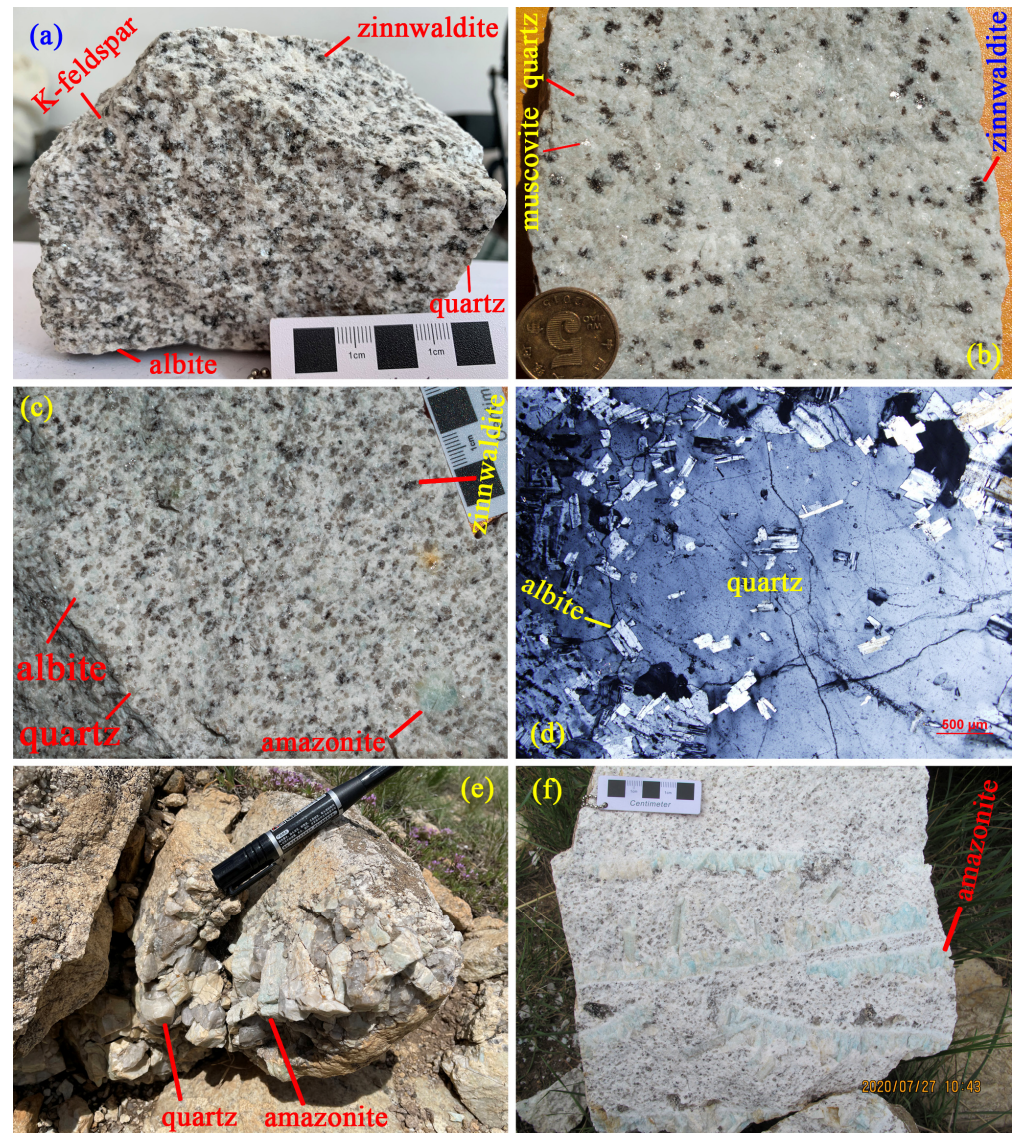


Figure 2. Lithologic character of the Shihuiyao granites: (a) zinnwaldite granite; (b) muscovite–zinnwaldite granite; (c) amazonite-bearing granite; (d) photomicrograph showing the snowball quartz in amazonite-bearing granite; (e) quartz–amazonite pegmatite; and (f) amazonite pegmatite.

In this study, stocks II–IV in the center were chosen as research objectives. The main lithology of stock III is zinnwaldite granite, which contains amazonite pegmatite veins. Two main lithologies predominate stock II: muscovite–zinnwaldite granite and amazonite-bearing granite, but there is no clear boundary between them (Figure 1b). Stock IV has been affected by late- and post-magmatic alterations, including greisenization and albitization, and quartz–amazonite pegmatites are very common throughout the stock. In most observed places, the granites are medium- to fine-grained, massive and equigranular.

The zinnwaldite granite mainly consists of quartz (30%–35%), K-feldspar (30%–35%), albite (20%–25%) and zinnwaldite (8%–10%) (Figure 2a). Zinnwaldite shows well-developed cleavage, parallel extinction and is slightly pleochroic from colorless to yellow-brown. Albite appears as narrow laths with polysynthetic twinning, usually intergrown with K-feldspar and quartz or wrapped by large quartz grains. K-feldspar is irregular, and the quartz exhibits characteristic undulose extinction. The muscovite–zinnwaldite is dominated by quartz (30%–35%), K-feldspar (30%–35%), albite (25%–30%), zinnwaldite (3%–5%) and some muscovite (Figure 2b). The dominant K-feldspar is microcline or perthite, and the quartz presents undulose extinction. Zinnwaldite occurs as a minor component, together with some muscovite. Albite occurs as small, tabular crystals, sometimes interspersed or embedded in large granular quartz. Amazonite-bearing granite is mainly composed of quartz (30%–35%), K-feldspar (35%–40%) (amazonite content is about 15%–20%), albite (25%–30%) and zinnwaldite (3%–5%) (Figure 2c). A hand specimen of amazonite has a light blue color. Zinnwaldite shows weak pleochroism and occurs sporadically. Small euhedral albite crystals are zonally arranged in the inner parts of quartz, showing snowball textures (Figure 2d). The quartz–amazonite pegmatite contains quartz and amazonite megacrysts up to 10 cm in size (Figure 2e). Locally, quartz is absent and amazonite occurs within the granites (Figure 2f). The monazite U–Pb age of the zinnwaldite granite was placed at 146.8 Ma [16] and 150.2 Ma [18], the monazite U–Pb age of amazonite-bearing granite was dated to 147.0 ± 1.7 Ma [16]. The monazite U–Pb age and ^{40}Ar – ^{39}Ar plateau age of mica from muscovite–zinnwaldite granite were 145–147.9 Ma [18] and 146.3 ± 1.1 Ma [16], respectively. Its main additional minerals are zircon and monazite, but manganocolumbite and cassiterite are also common (Figure 3), as well as some topaz crystals.

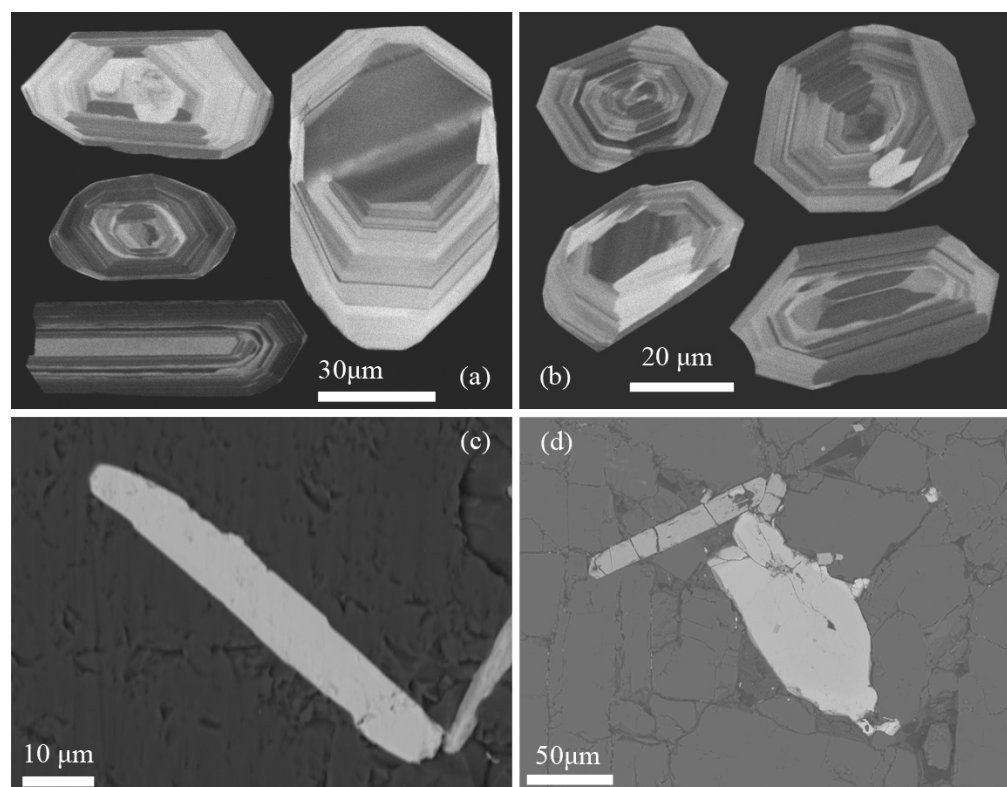


Figure 3. CL images of zircon within zinnwaldite granite (a) and amazonite-bearing granite (b) BSE images of manganocolumbite within muscovite–zinnwaldite granite (c) and amazonite-bearing granite (d).

3. Analytical Methods

3.1. Whole-Rock Major and Trace Element Analyses

Eleven samples were selected for bulk rock geochemical analyses. Fresh rock specimens were broken down into smaller fragments and then finely powdered in an agate swing mill to ~200 mesh. Element compositions were analyzed at the Key Laboratory of Mineral Resources Evaluation in Northeast Asia, Ministry of Natural Resources, Jilin University, Changchun, China. Major elements were determined via X-ray fluorescence spectrometer analysis on flat glass disks, which were obtained by fusing a mixture of rock powder and lithium metaborate. Acid-digested (HF, HNO₃) samples were used to search for trace elements in an Agilent 7500a ICP-MS. The analytical precision of this method was greater than 5% and 10% for major oxides and trace elements, respectively.

3.2. EPMA and LA-ICP-MS Analyses of Minerals

The chemical compositions of mica were analyzed using an electron microprobe (Shimadzu EPMA-1600) equipped with a wavelength dispersive spectrometer at the State Key Laboratory of Ore Deposit Geochemistry, Institute of Geochemistry, Chinese Academy of Sciences (IGCAS). The analytical conditions were as follows: 15 kV accelerating voltage, 10 nA beam current and 5 μm beam diameter. The analytical conditions were as follows: 15 kV accelerating voltage, 10 nA beam current and 5 μm beam diameter. The chemical compositions of Nb-Ta oxide mineral were analyzed using a JEOL JXA 8100 electron microprobe at the State Key Laboratory of Nuclear Resources and Environment of the East China University of Technology. The analytical conditions were as follows: 15 kV accelerating voltage, 20 nA beam current and 2 μm beam diameter. For mica, the standards biotite (K, Mg, Al, Si, Fe), kaersutite (Na, Ca, Ti, Mn), tugtupite (Cl) and apatite (F) were used. For Nb-Ta oxide mineral, the major standards were niobate (Nb), tantalide (Ta), magnetite (Fe) and bustamite (Mn). Detailed descriptions of this analytical technique are provided by Yang et al. [27] and Wang et al. [28].

Trace element concentrations of mica and feldspar were determined using an ELAN DRC-e ICP-MS coupled with a GeoLasPro 193 nm laser system at IGCAS. Helium was applied as a carrier gas, which was mixed with Argon via a T-connector before entering the ICP-MS. Each analysis incorporated a background acquisition of approximately 30 s (gas blank) followed by 50 s of data acquisition from the sample. The laser fluence, repetition rate and ablated spot size used for this study were 4–5 J/cm², 5–6 Hz and 44 μm, respectively. NIST glasses (SRM 610, 612) and USGS (BIR-1G, BHVO-2G, BCR-2G) were used as the external standards, and Si (determined by EPMA) was used as the internal standard. Analytical data were processed using software ICPMSDataCal [29]. The relative standard deviation of trace elements in Chinese geological standard glasses, CGSG-1 and CGSG-2, is smaller than 10%. Detailed descriptions of the analytical technique are provided by Tang et al. [30].

4. Results

4.1. Major and Trace Element Geochemistry

The data from Shihuiyao samples are listed in Table 1. The losses on ignition (LOIs) are relatively low (<0.5 wt%), confirming that these rocks are apparently unaffected, or have undergone only minor alterations. The SiO₂ contents of zinnwaldite, muscovite–zinnwaldite and amazonite-bearing granites are 75.78%–77.08%, 75.15%–75.72% and 73.66%–75.38%, respectively. TFe₂O₃ contents were 1.38%–1.71%, 1.03%–1.25% and 0.89%–1.00%, and Na₂O contents were 4.54%–4.81%, 4.50%–4.64% and 4.92%–6.27%, respectively. The amazonite-bearing granite has a relatively high content of Na₂O and Al₂O₃ compared to zinnwaldite granite and muscovite–zinnwaldite granite. The granites are slightly to mildly peraluminous ($A/CNK = \text{molar } (Al_2O_3)/(CaO + Na_2O + K_2O) = 1.06\text{--}1.16$; Figure 4a) and belong to high-K calc-alkaline series (Figure 4b). The total REE abundance (ΣREE) values are low and range from 32.83 ppm to 70.76 ppm. The REE patterns have pronounced negative Eu anomalies ($\delta\text{Eu} = 0.01\text{--}0.08$) and exhibit strong tetrad effects (M-type; Figure 5a). The

Shihuiyao granite is characterized by enrichments in Rb, Th, U, Nb and Ta and depletions in Ba, Sr, Ti and Y (Figure 5b). All these features are commonly observed in highly differentiated granitic rocks [16,18].

Table 1. Major (wt%) and trace element (ppm) data for the Shihuiyao granites.

Stock	III					II					
Lithology	Zinnwaldite Granite				Muscovite–Zinnwaldite Granite			Amazonite-Bearing Granite			
Sample	TC3-1	TC3-3	TC3-5	TC3-8	20S60-6	20S60-3	20S61-4	20S61-1	20S61-7	20S61-9	20S60-8
SiO ₂	74.95	76.51	77.08	77.03	75.78	75.15	75.72	73.66	75.38	74.58	73.82
TiO ₂	0.02	0.02	0.01	0.02	0.02	0.02	0.01	0.01	0.01	0.01	0.02
Al ₂ O ₃	13.75	12.78	12.84	12.69	12.90	13.60	13.43	14.88	13.91	14.28	14.23
TFe ₂ O ₃	1.71	1.47	1.38	1.62	1.71	1.03	1.25	0.89	0.90	1.00	1.03
MnO	0.19	0.14	0.13	0.16	0.17	0.13	0.17	0.12	0.13	0.16	0.12
MgO	0.05	0.05	0.02	0.04	0.04	0.03	0.02	0.03	0.03	0.08	0.05
CaO	0.14	0.12	0.15	0.17	0.19	0.16	0.08	0.10	0.08	0.08	0.19
Na ₂ O	5.50	4.81	4.75	4.62	4.54	4.64	4.50	6.27	4.92	5.58	5.12
K ₂ O	3.09	3.55	3.53	3.76	3.70	4.23	3.68	3.22	3.87	3.63	4.05
P ₂ O ₅	0.02	0.02	0.01	0.03	0.01	0.01	0.01	0.01	0.02	0.02	0.01
LOI	0.36	0.22	0.30	0.34	0.41	0.41	0.46	0.21	0.39	0.42	0.50
Total	99.77	99.69	100.19	100.46	99.47	99.41	99.33	99.41	99.63	99.84	99.14
A/CNK	1.09	1.07	1.08	1.06	1.09	1.09	1.16	1.06	1.12	1.08	1.08
A/NK	1.11	1.09	1.10	1.09	1.12	1.11	1.18	1.08	1.13	1.09	1.11
DI	95.45	96.26	96.20	95.94	95.25	96.40	95.64	97.11	96.61	96.76	96.33
La	6.28	4.70	6.50	3.21	4.95	3.02	3.80	3.63	3.19	4.07	3.96
Ce	20.68	17.85	19.62	12.02	17.04	12.07	13.12	13.09	11.91	13.87	16.18
Pr	3.43	2.42	3.38	1.83	2.64	1.58	1.72	1.91	1.63	1.95	2.21
Nd	12.05	8.42	12.08	7.21	9.62	5.66	5.29	6.12	4.87	6.06	8.38
Sm	4.58	3.48	4.75	3.34	4.19	2.73	2.10	2.74	1.80	2.36	4.16
Eu	0.03	0.08	0.09	0.07	0.02	0.01	0.01	0.02	0.01	0.02	0.01
Gd	3.28	2.84	3.36	2.84	3.12	2.21	1.44	2.00	1.10	1.63	3.69
Tb	0.90	0.87	0.91	0.85	0.88	0.65	0.43	0.66	0.33	0.52	1.03
Dy	6.08	5.86	5.51	5.53	5.94	4.61	3.06	4.72	2.31	3.64	7.27
Ho	1.23	1.22	1.09	1.14	1.13	0.88	0.56	0.91	0.44	0.70	1.42
Er	4.10	3.95	3.40	3.61	3.86	2.90	1.93	3.15	1.59	2.38	4.59
Tm	0.83	0.81	0.72	0.74	0.79	0.61	0.40	0.66	0.35	0.52	0.88
Yb	6.37	5.70	4.96	5.39	6.04	4.86	3.26	5.42	2.90	4.22	6.74
Lu	0.92	0.85	0.74	0.79	0.85	0.66	0.45	0.73	0.40	0.59	0.96
∑REE	70.76	59.05	67.09	48.55	61.07	42.43	37.56	45.76	32.83	42.53	61.47
δEu	0.03	0.08	0.06	0.07	0.01	0.01	0.02	0.02	0.02	0.03	0.01
(La/Yb) _N	0.65	0.54	0.86	0.39	0.54	0.41	0.77	0.44	0.72	0.64	0.39
TE _{1,3}	1.33	1.41	1.30	1.36	1.36	1.43	1.46	1.47	1.47	1.45	1.40
Rb	954	946	891	997	1094	1364	1253	1405	1651	1587	1278
Ba	6.88	11.25	6.01	13.21	8.59	3.78	8.09	10.30	5.06	6.77	5.71
Th	12.46	8.35	8.62	8.05	7.80	6.40	7.74	9.03	8.58	9.12	7.98
U	1.84	3.87	2.50	3.13	2.97	3.01	0.45	0.51	0.63	0.69	0.73
Nb	31.06	36.32	36.23	33.24	36.13	53.41	42.90	57.33	69.29	66.52	30.08
Ta	12.83	13.56	14.36	12.46	11.38	18.77	17.80	14.27	24.09	14.34	8.86
Sr	3.24	4.71	4.80	3.68	2.77	4.29	2.92	1.71	1.48	1.62	2.88
Zr	86.07	48.86	52.70	59.58	48.56	43.26	28.61	47.24	36.09	47.77	37.68
Hf	10.66	6.11	6.48	6.77	6.26	6.38	4.77	7.34	5.94	6.56	5.47
Y	10.28	11.04	10.08	9.76	10.51	7.28	3.79	5.79	2.79	4.49	14.17
Ga	33.40	31.93	28.69	30.33	33.55	35.69	26.36	39.58	36.62	37.58	34.05
Li	535	432	384	443	500	555	711	729	799	849	520
Be	4.56	4.09	4.27	4.39	4.84	5.50	6.81	10.56	7.54	10.15	17.28
Pb	29.24	36.71	42.17	30.53	75.47	37.82	33.03	46.68	44.15	45.69	51.41
Sc	8.69	8.15	5.43	5.30	9.98	5.37	8.50	6.39	6.93	6.65	5.38
V	2.45	3.62	2.34	2.72	3.99	2.18	1.68	2.02	2.03	2.03	2.56
Cr	5.85	16.15	18.31	6.22	6.18	3.93	14.15	3.70	3.18	5.37	24.59
Co	0.59	1.02	0.59	0.96	0.54	0.42	0.65	0.49	0.37	0.53	0.70
Ni	3.10	4.07	3.27	3.48	2.49	1.44	10.52	1.31	1.22	2.88	7.99
Cs	38	29	27	28	67	35	51	68	59	79	63
10,000 Ga/Al	4.59	4.72	4.22	4.52	4.91	4.96	3.71	5.03	4.97	4.97	4.52
Zr/Hf	8.07	8.00	8.14	8.80	7.76	6.78	5.99	6.44	6.07	7.28	6.88
K/Rb	26.88	31.14	32.82	31.28	28.06	25.73	24.37	19.02	19.43	18.98	26.30

Table 1. Cont.

Stock	III					II					
Lithology	Zinnwaldite Granite					Muscovite–Zinnwaldite Granite			Amazonite-Bearing Granite		
Sample	TC3-1	TC3-3	TC3-5	TC3-8	20S60-6	20S60-3	20S61-4	20S61-1	20S61-7	20S61-9	20S60-8
Nb/Ta	2.42	2.68	2.52	2.67	3.17	2.85	2.41	4.02	2.88	4.64	3.40
Ti/Zr	1.18	2.58	1.14	2.31	1.85	2.77	2.72	1.78	1.66	1.63	2.71
Ti/Y	9.92	11.40	5.95	14.13	8.56	16.47	20.55	14.50	21.52	17.35	7.19
Th/Ce	0.60	0.47	0.44	0.67	0.46	0.53	0.59	0.69	0.72	0.66	0.49
Th/La	1.98	1.78	1.33	2.51	1.58	2.12	2.03	2.49	2.69	2.24	2.02
T _{Zr}	740 °C	698 °C	704 °C	712 °C	699 °C	689 °C	666 °C	691 °C	724 °C	694 °C	677 °C

A/CNK = molar ratio of Al₂O₃/(CaO + Na₂O + K₂O); A/NK = molar ratio of Al₂O₃/(Na₂O + K₂O); DI = differentiation index; δEu = 2Eu_N/(Sm_N + Gd_N); (La/Yb)_N is La/Yb ratio that is normalized to chondritic values. Bulk-rock zirconium saturation temperature (T_{Zr}) was calculated using Watson and Harrison equation [37]: T_{Zr} = 12,900/[2.95 + 0.85 × M + ln(496,000/Zr_{melt})] – 273.15, where M = molar [(Na + K + 2 × Ca)/(Al × Si)], Zr_{melt} = the concentration (ppm) of Zr in whole rock. The degree of the tetrad effect (TE_{1,3}) was calculated using the formulae of Irber: TE_{1,3} = (t1 × t3)^{0.5}, where t1 = (Ce/Ce^t × Pr/Pr^t)^{0.5} and t3 = (Tb/Tb^t × Dy/Dy^t)^{0.5}, with Pr/Pr^t = Pr_N/(La_N^{1/3} × Nd_N^{2/3}), Tb/Tb^t = Tb_N/(Gd_N^{2/3} × Ho_N^{1/3}) and Dy/Dy^t = Dy_N/(Gd_N^{1/3} × Ho_N^{2/3}).

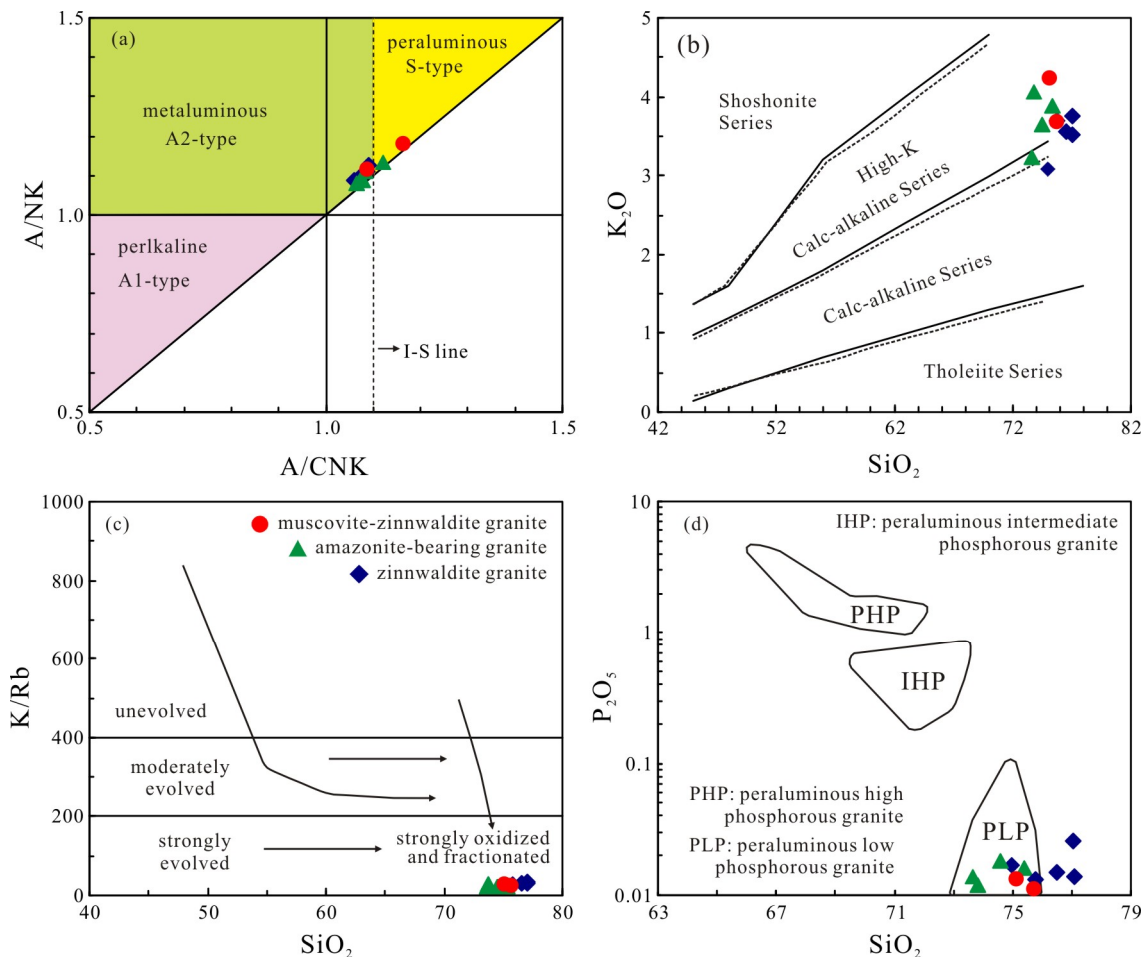


Figure 4. (a) A/CNK vs. A/NK plot (after [31,32]); (b) SiO₂ vs. K₂O diagram (after [33]); (c) K/Rb vs. SiO₂ plot (after [34]); (d) SiO₂ vs. P₂O₅ diagram (after [31]).

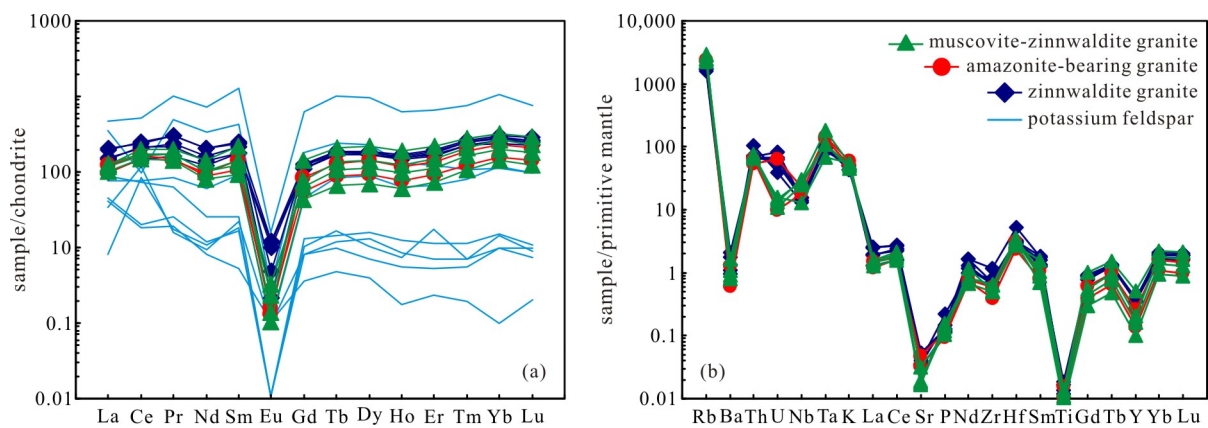


Figure 5. REE patterns (a) and trace element spider diagrams (b) for the Shihuiyao granites. Normalization values are taken from [35,36].

4.2. Mineral Chemistry

The chemical compositions of mica and feldspar, as well as columbite-group minerals, are listed in Tables 2–4.

EPMA analyses indicate that the silica and fluorine contents of zinnwaldite of zinnwaldite granite (42.16%–46.18%, 4.14%–5.31%) are lower than those of muscovite–zinnwaldite granite (46.55%–49.88%, 6.32%–7.25%), amazonite-bearing granite (47.58%–50.84%, 6.40%–7.67%) and pegmatite (47.03%–53.19%, 6.57%–7.17%) (Figure 6a). Their FeO contents are 12.24%–16.14%, 8.73%–11.10%, 7.97%–9.06%, and 7.98%–9.37% (Figure 6b), respectively. LA-ICP-MS analyses indicate that Rb is the most abundant minor element in K-feldspar. The concentration of Rb varies from 3072 to 7635 ppm and the Cs content varies from 15 to 149 ppm. Rb (12,742–18,825 ppm) and Li (16,717–33,332 ppm) are abundant in the zinnwaldite and show a positive relationship (Figure 6c). Zinnwaldite contains 50 to 394 ppm Nb and 13 to 110 ppm Ta. Overall, mica from zinnwaldite granite has slightly higher contents of Nb and Ta (Figure 6d,e), and relatively lower contents of Rb and Li, compared to that from amazonite-bearing granite.

Columbite-group minerals are observed in the muscovite–zinnwaldite granite and amazonite-bearing granite. They occur as scattered tabular or prismatic subhedral grains up to 200 μm long (Figure 3c,d), disseminated between quartz, K-feldspar, zinnwaldite and albite. The Columbite-group minerals have narrow content ranges of MnO (10.54–12.64 wt%), FeO (8.16–10.63 wt%), Nb₂O₅ (66.60–71.89 wt%) and Ta₂O₅ (6.13–12.64 wt%), belonging to manganocolumbite with high Mn[#] (atomic Mn/(Mn + Fe) ratio) and low Ta[#] (atomic Ta/(Ta + Nb) ratio) (Figure 6f).

Table 2. Major element data (wt%) for zinnwaldite of Shihuiyao granites.

Lithology	SiO ₂	TiO ₂	Al ₂ O ₃	FeO	MnO	MgO	CaO	Na ₂ O	K ₂ O	Cl	F	Total
zinnwaldite granite	43.43	0.07	24.01	15.45	1.45	-	-	0.23	9.80	0.01	4.58	97.10
	45.45	0.05	23.59	13.23	1.27	-	-	0.18	9.78	0.01	5.31	96.64
	44.41	0.03	23.46	14.36	1.35	-	-	0.21	9.79	0.01	5.11	96.57
	45.33	0.05	23.09	13.43	1.28	-	-	0.13	9.94	-	5.19	96.26
	46.18	0.02	23.99	12.24	1.22	-	-	0.14	9.80	-	4.82	96.36
	42.13	0.01	24.50	15.55	1.41	-	-	0.17	9.74	-	4.50	96.11
	42.49	0.06	23.44	15.76	1.44	-	-	0.06	9.78	-	4.78	95.79
	42.30	0.05	24.22	16.14	1.37	-	-	0.17	9.76	-	4.64	96.70
	42.58	0.06	24.06	15.70	1.34	-	-	0.14	9.75	0.01	4.47	96.23
	42.35	0.02	23.71	15.56	1.41	-	-	0.14	9.78	0.01	4.61	95.64
	42.87	0.06	24.05	15.96	1.43	-	-	0.13	9.76	0.01	5.03	97.17
	42.16	-	24.85	15.61	1.49	-	-	0.09	9.84	-	4.14	96.44
	42.21	-	24.32	15.62	1.50	-	-	0.10	9.77	0.01	4.87	96.35

Table 2. Cont.

Lithology	SiO ₂	TiO ₂	Al ₂ O ₃	FeO	MnO	MgO	CaO	Na ₂ O	K ₂ O	Cl	F	Total
muscovite–zinnwaldite granite	47.25	0.01	22.61	10.55	1.58	-	-	0.26	9.82	-	6.73	95.99
	47.37	0.06	22.04	10.38	1.61	-	-	0.18	9.86	0.01	6.69	95.37
	47.63	0.06	22.28	10.34	1.59	-	-	0.31	9.88	-	6.82	96.04
	47.41	0.01	22.04	10.52	1.73	-	-	0.18	9.84	0.01	6.46	95.47
	48.06	0.02	22.00	10.23	1.54	-	-	0.12	9.81	0.01	6.73	95.69
	48.68	-	21.71	10.10	1.50	-	-	0.19	9.79	-	6.78	95.89
	48.04	0.02	21.95	10.08	1.50	-	0.02	0.04	9.92	-	6.61	95.40
	48.05	0.04	22.18	9.66	1.46	-	-	0.08	10.05	0.01	6.56	95.32
	49.88	0.02	20.87	8.73	1.29	-	-	0.02	9.83	-	7.25	94.83
	46.55	0.01	22.82	11.10	1.63	-	-	0.21	9.75	-	6.32	95.72
	47.49	0.04	22.49	10.42	1.64	-	-	0.26	9.89	0.01	6.70	96.11
	48.20	0.02	21.59	9.63	1.43	-	-	0.17	9.92	-	6.46	94.69
	47.45	0.03	22.02	10.33	1.53	0.01	-	0.20	9.87	-	6.49	95.19
49.19	-	21.52	9.50	1.51	-	-	0.15	10.05	0.01	7.01	95.99	
amazonite-bearing granite	50.84	-	20.53	8.08	1.53	-	-	0.22	9.90	0.01	7.30	95.33
	50.29	0.01	21.23	8.35	1.74	-	-	0.19	9.91	-	7.10	95.84
	50.23	-	21.01	7.97	1.56	-	-	0.17	9.91	-	7.44	95.17
	50.58	0.02	21.08	8.47	1.58	-	-	0.17	9.96	0.02	6.95	95.90
	49.83	-	21.22	8.52	1.62	-	-	0.25	9.83	0.01	6.90	95.26
	49.59	-	19.94	8.22	1.50	-	-	0.11	10.08	0.02	6.75	93.35
	49.48	0.01	20.06	8.01	1.49	-	-	0.12	9.89	-	6.75	92.98
	48.81	0.05	22.23	9.06	1.84	-	-	0.13	9.87	0.01	7.67	96.44
	50.23	-	21.10	8.58	1.70	-	-	0.12	10.13	-	7.18	96.02
	48.54	0.01	21.14	8.94	1.84	-	-	0.10	9.83	-	6.80	94.34
47.58	-	20.83	8.77	1.65	-	-	0.11	9.91	0.01	6.40	92.54	
pegmatite	48.53	0.02	21.60	8.88	1.68	-	-	0.09	9.91	-	7.12	94.83
	47.70	-	22.13	9.37	1.93	-	-	0.16	9.85	0.01	6.82	95.09
	49.77	0.03	21.20	8.31	1.64	-	-	0.17	9.99	-	7.05	95.18
	47.49	-	21.47	9.02	1.81	-	-	0.12	9.90	-	6.80	93.74
	47.03	-	20.41	8.43	1.62	-	-	0.13	10.00	0.01	6.57	91.42
	50.31	0.01	21.40	8.55	1.69	-	-	0.18	9.93	-	7.16	96.21
	49.62	0.03	21.17	8.64	1.69	-	-	0.20	9.94	-	6.85	95.25
	50.40	0.01	21.34	8.35	1.63	-	-	0.21	9.79	-	7.14	95.85
53.19	-	21.36	7.98	1.60	-	-	0.23	9.64	0.01	7.17	98.16	

Table 3. Trace element data (ppm) for potassium feldspar and zinnwaldite of Shihuiyao granites.

Lithology	Zinnwaldite Granite		Muscovite–Zinnwaldite Granite		Amazonite-Bearing Granite			Zinnwaldite Granite			Muscovite–Zinnwaldite Granite		Amazonite-Bearing Granite				
	Potassium Feldspar																
Minerals	Zinnwaldite																
Li	1.98	1.96	0.86	2.57	0.33	5.25	2.29	1.00	18,964	17,127	16,717	27,297	25,809	26,722	33,332	32,256	31,960
Be	0.38	0.10	4.48	6.11	5.58	4.96	2.80	6.74	20.3	13.6	13.1	64.7	43.8	63.9	123	124	86.0
P	43.4	45.7	73.0	9.90	13.9	34.4	77.5	91.2	5.05	37.6	32.3	37.5	49.1	21.2	13.7	50.2	13.6
Sc	0.92	1.00	0.77	0.89	1.34	0.61	1.86	1.08	252	290	256	196	231	179	203	198	224
Ga	47.5	47.3	48.2	47.8	63.9	49.6	47.7	49.9	158	178	192	104	97.7	70.1	109	77.5	107
As	0.57	0.44	0.76	4.83	2.40	0.57	0.74	0.90	0.15	0.38	0.48	0.05	0.11	0.09	0.14	0.00	0.23
Rb	4008	4112	5764	3072	2534	6040	5240	6735	13,526	13,275	12,742	15,438	15,065	14,736	18,496	17,970	18,825
Sr	0.86	0.56	0.56	0.70	2.45	0.81	1.37	0.45	0.05	0.14	0.46	0.11	0.31	0.13	0.03	0.34	0.61
Y	1.29	0.79	0.32	0.21	8.17	0.10	31.13	3.26	0.01	0.29	0.37	0.02	0.16	0.01	0.00	0.05	0.00
Zr	0.26	0.19	0.33	0.01	6.49	0.00	2.95	2.59	0.07	0.27	4.57	0.31	1.12	0.14	0.06	0.80	0.22
Nb	0.15	0.83	0.03	0.00	0.29	0.02	0.24	0.24	216	303	394	136	141	66.2	50.2	56.4	125
Ag	0.09	0.27	0.04	0.25	0.02	0.00	0.06	0.04	0.00	0.00	0.01	0.01	0.01	0.02	0.00	0.02	0.01
Sn	1.03	1.07	7.87	7.32	4.32	8.80	5.98	8.04	237	360	397	47.8	92.4	39.1	36.0	44.5	71.7
Cs	30.0	27.5	14.7	17.4	39.2	24.8	33.4	55.3	1667	1176	907	3104	1239	3018	2815	3651	1269
Ba	7.40	3.29	6.33	3.72	7.76	4.64	16.3	9.56	1.65	1.66	2.50	3.28	3.17	2.81	2.16	2.16	14.1
La	0.25	1.08	1.44	1.32	11.2	2.76	14.7	2.36	0.00	0.12	0.02	0.01	0.01	0.00	0.00	0.01	0.00
Ce	6.74	9.34	1.65	1.46	7.79	5.91	42.5	6.14	0.01	0.15	0.04	0.01	0.02	0.00	0.00	0.00	0.00
Pr	0.20	0.18	0.29	0.21	5.55	0.71	11.2	0.94	0.00	0.09	0.01	0.00	0.01	0.00	0.00	0.00	0.00
Nd	0.64	0.56	0.71	0.49	20.4	1.51	43.6	3.63	0.00	0.36	0.06	0.01	0.03	0.00	0.00	0.00	0.00
Sm	0.35	0.42	0.33	0.10	8.24	0.49	24.7	1.75	0.00	0.16	0.03	0.00	0.00	0.00	0.00	0.02	0.00
Eu	0.00	0.01	0.00	0.01	0.02	0.00	0.11	0.01	0.01	0.00	0.00	0.00	0.00	0.00	0.00	0.00	0.00
Gd	0.33	0.21	0.21	0.10	4.72	0.26	16.1	1.16	0.00	0.11	0.10	0.00	0.02	0.01	0.00	0.01	0.02
Tb	0.07	0.06	0.05	0.02	1.16	0.08	5.02	0.41	0.00	0.03	0.03	0.00	0.00	0.00	0.00	0.00	0.00
Dy	0.51	0.43	0.23	0.13	7.45	0.33	32.00	2.85	0.00	0.15	0.12	0.01	0.06	0.00	0.00	0.02	0.01
Ho	0.09	0.06	0.04	0.01	0.97	0.06	4.67	0.46	0.00	0.01	0.04	0.00	0.01	0.00	0.00	0.01	0.01
Er	0.24	0.15	0.11	0.05	2.61	0.38	14.28	1.42	0.00	0.07	0.11	0.01	0.03	0.01	0.00	0.02	0.00
Tm	0.04	0.02	0.02	0.01	0.34	0.02	2.39	0.25	0.00	0.01	0.02	0.00	0.01	0.00	0.00	0.01	0.00

Table 3. Cont.

Lithology	Zinnwaldite Granite			Muscovite–Zinnwaldite Granite			Amazonite-Bearing Granite			Zinnwaldite Granite			Muscovite–Zinnwaldite Granite			Amazonite-Bearing Granite		
Minerals	Potassium Feldspar									Zinnwaldite								
Yb	0.32	0.29	0.21	0.02	2.37	0.20	22.0	2.40	0.01	0.14	0.22	0.02	0.06	0.05	0.00	0.06	0.01	
Lu	0.04	0.03	0.02	0.01	0.31	0.03	2.39	0.32	0.00	0.01	0.04	0.01	0.01	0.00	0.00	0.00	0.01	
Hf	0.04	0.04	0.08	0.00	0.84	0.00	0.54	0.50	0.05	0.16	2.25	0.18	0.65	0.03	0.08	0.37	0.17	
Ta	0.04	0.07	0.02	0.00	0.09	0.01	0.08	0.11	87.9	83.0	110	46.1	52.6	31.4	12.6	58.2	33.6	
W	0.02	0.04	0.00	0.63	0.02	0.05	0.08	0.23	30.9	27.7	26.5	24.6	20.3	26.4	11.3	25.0	27.5	
Au	0.00	0.00	0.01	0.00	0.01	0.00	0.00	0.00	0.07	0.03	0.08	0.04	0.06	0.02	0.02	0.07	0.01	
Bi	0.13	0.15	1.31	0.08	2.70	0.02	0.82	0.32	0.00	0.02	0.05	0.04	0.36	0.02	0.00	0.09	0.01	
Pb	23.0	72.6	111	182	78.4	142	82.5	69.6	7.36	7.80	9.73	8.21	9.80	8.37	7.49	8.45	6.78	
Th	0.26	0.38	0.11	0.02	8.83	0.00	0.68	0.92	0.01	0.32	0.44	0.01	0.03	0.00	0.00	0.04	0.00	
U	0.01	1.66	0.00	0.00	0.07	0.00	0.14	0.04	0.00	0.01	0.03	0.00	0.01	0.00	0.00	0.01	0.00	
Rb ₂ O	0.44%	0.45%	0.63%	0.34%	0.28%	0.66%	0.57%	0.74%	1.48%	1.45%	1.39%	1.69%	1.65%	1.61%	2.02%	1.97%	2.06%	

Table 4. Major element data (wt%) for columbite-group minerals of Shihuiyao granites.

Lithology	Muscovite–Zinnwaldite Granite			Amazonite-Bearing Granite				
Al ₂ O ₃	0.01	0.10	0.00	0.05	0.03	0.00	0.04	0.01
SnO ₂	0.05	0.07	0.06	0.03	0.07	0.07	0.12	0.00
Nb ₂ O ₅	71.89	68.58	71.13	70.39	66.60	67.88	68.89	68.36
Ta ₂ O ₅	6.13	9.25	7.65	8.66	11.02	10.46	9.80	12.64
TiO ₂	1.71	1.32	0.49	0.60	1.15	1.04	1.19	0.56
WO ₃	0.93	0.38	1.65	0.20	0.50	0.24	0.78	0.46
CaO	0.02	0.26	0.01	0.02	0.02	0.02	0.02	0.00
FeO	9.31	8.97	10.63	8.55	8.31	8.16	8.37	8.19
MnO	11.52	11.66	10.54	12.14	12.13	12.26	12.24	12.64
Total	101.55	100.59	102.16	100.63	99.81	100.13	101.45	102.86
Ta/(Ta + Nb)	0.05	0.08	0.06	0.07	0.09	0.08	0.08	0.10
Mn/(Mn + Fe)	0.56	0.57	0.50	0.59	0.60	0.60	0.60	0.61

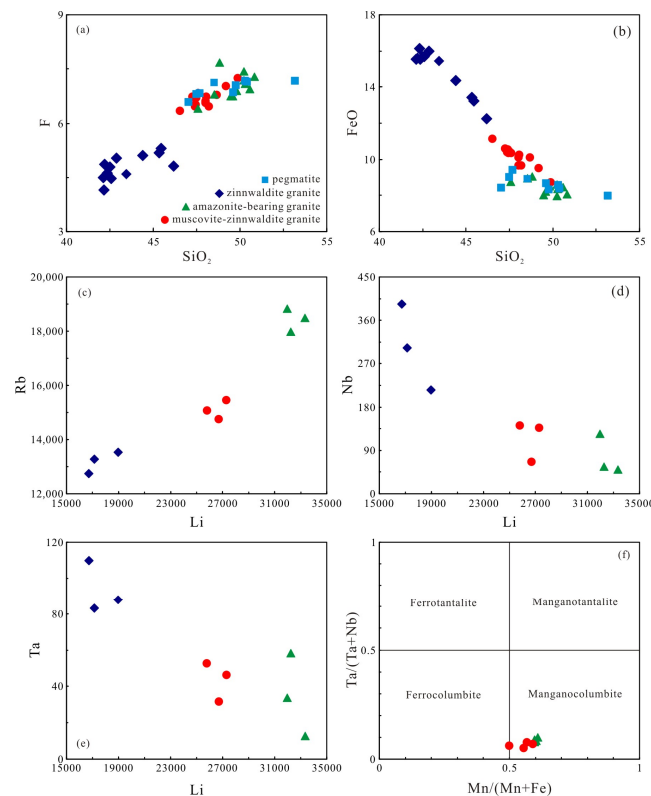


Figure 6. SiO₂ vs. F (a), FeO (b) and Li vs. Rb (c), Nb (d), and Ta (e) diagrams for the zinnwaldite of Shihuiyao granites. (f) Atomic Ta/(Nb + Ta) ratios vs. atomic Mn/(Mn + Fe) ratios of columbite-group minerals.

5. Petrogenesis of Shihuiyao Granites

5.1. Classification: Low-P Peraluminous Rare-Metal Granite

Rare-metal granites can be classified into three main groups (peralkaline, metaluminous to peraluminous low-P and peraluminous high-P rare-metal granites) based on their lithological–geochemical peculiarities, protolith compositions and tectonic properties [38]. Low molar $\text{Al}_2\text{O}_3/[\text{Na}_2\text{O} + \text{K}_2\text{O}]$ values ($A/NK < 1$) and high Zr and Th contents are major geochemical indications of peralkaline rare-metal granites [31]. These granites are relatively rich in Fe and contain sodic amphiboles and/or pyroxene, which correspond to the A1-type granites of Eby [39]. The Shihuiyao granite samples exhibit high A/NK values (1.09–1.18), relatively low Zr and Th contents, and do not contain mafic alkaline minerals, in contrast to the peralkaline rare-metal granites. Peraluminous, high-P, rare-metal granites are generally associated with strongly peraluminous muscovite-biotite leucogranitic plutons with $A/NK > 1.15$, equivalent to S-type granite [31,40]. The Shihuiyao granite samples exhibit low A/CNK values (mostly < 1.1) and low P_2O_5 contents (0.01–0.02 wt%), different from S-type granites. Weakly peraluminous calc-alkaline Shihuiyao granites can be defined as low-P, peraluminous, rare-metal granites, which correspond to the I- and A2-type granites of Eby [39].

The Shihuiyao granite samples are high-silica ($\text{SiO}_2 = 73.66\text{--}77.08$ wt%) and alkali-rich ($\text{K}_2\text{O} + \text{Na}_2\text{O} = 8.18\text{--}9.49$ wt%) rocks. They contain moderately high concentrations (in ppm) of Rb (891–1651), Cs (27–79) and Li (384–849), and relatively low contents of MgO, CaO and TiO_2 (< 0.06 wt%). These characteristics that indicate the studied granites experience strong magmatic differentiation. Their high differentiation indexes ($DI = 95\text{--}97$), Rb/Sr ratios and low K/Rb ratios highlight the high fractionation features of the granitic magmas. The highly evolved nature of the granites was also confirmed by the SiO_2 versus K/Rb diagram (Figure 4c). The Shihuiyao granites have low Zr/Hf (5.99–8.80) and Nb/Ta (2.41–4.64) ratios similar to highly evolved rare-metal granites (Figure 5a) [41]. The Shihuiyao granites also have low total REE contents (32.83–70.76 ppm) and pronounced REE tetrad effects. Overall, the Shihuiyao granites share similarities with the peraluminous, low-phosphorous (PLP), rare-metal granites (Figure 4d) of Linnen and Cuney [31].

5.2. Magma Source

Three petrogenetic models can explain the origin of highly evolved granites: (1) partial melting of crust materials [42,43]; (2) differentiation of more primitive magmas [44]; and (3) mixing between primitive and evolved magmas [45]. Lithologies ranging from relatively primitive to more evolved products would be expected if granites were the differentiation products of more primitive magmas. Mafic–intermediate igneous rocks and less-fractional felsic rocks are not present in the Shihuiyao area (Figure 1b). Therefore, the second model may not be suitable for the genesis of Shihuiyao granite. In addition, structures such as mafic–intermediate magmatic enclaves that indicate magma mingling and mixing have not been observed. Mineral textures such as resorbed cores and discordant zoning, as well as mafic clots characterizing magma mixing processes, are not present within the Shihuiyao granites, making the magma-mixing hypothesis less probable. More recently, Zhou et al. [16] measured the bulk-rock Li isotopes of the Shihuiyao granites, and homogeneous $\delta^7\text{Li}$ values indicated their derivation from the same magma source.

The Shihuiyao granites display enrichment in Rb, Li and K, and depletion in Ba, Sr, P, Ti, Mg and Ca, suggesting a continental crust origin [46]. They have high SiO_2 contents (73.66–77.08 wt%) and $\text{Mg}^\#$ values (2–14), consistent with crust-derived melts [47]. Low Ti/Zr (1.14–2.77) and Ti/Y (5.95–21.52) ratios are also similar to the crustal values (< 20 and < 200 , respectively) [48]. The Th/Ce (0.44–0.69) and Th/La (1.33–2.69) ratios of Shihuiyao granites are higher than primitive mantle rocks (0.02–0.05 and 0.12, respectively) but similar to crustal rocks (> 0.15 and > 0.30 , respectively) [36,49,50]. These geochemical characteristics indicate that Shihuiyao granites possibly derive from the partial melting of crust materials. Duan et al. [18] recently measured the Nd isotopic composition of monazite and whole-rock samples. All granites and monazites have similar Sm–Nd isotopic compositions, with $\epsilon_{\text{Nd}}(t)$

values ranging from +0.34 to +3.4, and - two-stage Nd isotopic model ages are in the range of 648–877 Ma. Therefore, the Shihuiyao granites were mainly generated via the melting of the Neoproterozoic juvenile crust.

6. Differentiation Sequence of Highly Fractionated Granitic Rocks in Shihuiyao Deposit

Shihuiyao granites exhibit an M-type REE tetrad effect (Figure 4a), and three models have been proposed for this tetrad effect: (1) fluoride–silicate liquid immiscibility [51]; (2) late-stage fluid/melt interactions, in particular with F-rich fluids [41]; and (3) fractionation of the REE during magma evolution [52]. The first model assumes that the separation of an immiscible fluoride melt with W-type patterns leaves behind residual melt with M-type patterns. However, a concave tetrad effect mirroring the pattern of the whole-rock samples was not observed in fluorite [14]. Instead, the REE patterns of the granites have an M-type tetrad effect in both whole-rock samples and in rock-forming minerals (such as K-feldspar) (Figure 5a) as well as accessory minerals (fluorite) [14]. This feature is clearly magmatic, inherited from the REE bulk composition of the residual melt. In addition, interstitial crystallization of fluorite and topaz among mica and albite indicates the F-rich nature of late-stage magmas. This texture is inconsistent with an immiscible fluoride melt. Hydrothermal interactions tend to decrease the Zr/Hf ratios with the increasing fluid interaction [53]; however, the Shihuiyao rocks exhibit no Zr/Hf variations or very little variations between the three granite types (Figure 7a). The zircon crystals of the Shihuiyao granites are pristine magmatic zircon (not metamict, nor altered) with oscillatory growth zoning (Figure 3a,b). Therefore, it is proposed that the tetrad effect was likely controlled by fractional crystallization rather than melt–fluid interactions. The lanthanide “tetrad effect” parameter ($TE_{1,3}$) can also be a useful geochemical fingerprint of highly fractionated granites, and the increase in $TE_{1,3}$ values varies with magmatic differentiation [54]. The Shihuiyao muscovite–zinnwaldite granite and amazonite-bearing granite show slightly higher $TE_{1,3}$ values but comparable K/Rb and Nb/Ta ratios to those of the zinnwaldite granite (Figure 7b,c), indicating the increasing degree of magma differentiation.

Mineralogical features and geochemical data indicate that the Shihuiyao granites experienced strong fractional crystallization during their magma evolution. Rock-forming minerals such as feldspars and micas can provide information on the magmatic evolution of granite systems. Rubidium is incompatible with granitic melt and is preferably substituted for K in mica or K-feldspar [55,56]. High Rb concentrations in these potassium-bearing minerals indicate granite fractionation, with decreasing K/Rb ratios indicating fractionation (Figure 7d) [57]. In the Shihuiyao granites, Rb is mainly hosted by micas, and to a minor degree in K-feldspar. Rb_2O concentrations of micas and K-feldspar increase from the zinnwaldite granite (1.39~1.48 wt%; 0.44~0.45 wt%) through to the muscovite–zinnwaldite granite (1.61~1.69 wt%; 0.28~0.63 wt%), and then to the amazonite-bearing granite (1.97~2.06 wt%; 0.57~0.74 wt%), with increasing fractionation (Figure 6c and Table 3). This process has also been measured using a Rayleigh fractionation model. Sample TC3-5 with the lowest Rb content was chosen to represent the parent melt. The estimated fractionating minerals and their relative proportions are 34.93% quartz, 30% K-feldspar, 25% plagioclase, 10% biotite and 0.07% monazite. The Rb–Sr, Rb–Cs and La–Ce trace element modeling shows that the evolutionary trajectories match very well with the bulk compositions of the Shihuiyao granites (Figure 7e–g). Experimental studies show that the presence of flux components such as Li and F will facilitate magmatic evolutionary processes and enhance crystal–melt fractionation [58]. Fluorine is the most abundant and compatible volatile element in highly evolved granitic magmas. The composition of residual granite melt during crystallization differentiation usually experiences an increase in fluorine content accompanied by a decrease in silica content [59,60], thereby resulting in the early crystallization of quartz and the development of a distinctive snowball texture, and an increase in sodium because of the shift of the granite eutectic in the Q–Ab–Or diagram. An increase in fluorine content also leads to a decrease in magma temperature [61].

The Shihuiyao granites have a characteristic snowball texture and higher Li and F contents, exhibiting a decrease in silica content with increasing fluorine content [15]. The F content of zinnwaldite also shows a linear increasing trend from zinnwaldite granite to muscovite–zinnwaldite granite, amazonite-bearing granite and pegmatite. The whole-rock zircon saturation temperatures (T_{Zr}) [37] of the muscovite–zinnwaldite granite and amazonite-bearing granite (666–694 °C) are slightly lower than those of the zinnwaldite granite (698–740 °C), reflecting different degrees of magma differentiation. These characteristics indicate their crystallization from highly evolved, F-rich, rare-metal-bearing granitic melts.

The magmatic evolution of granitic melts contributing to rare-metal mineralizations can be evaluated using the additional petrogenetic indices, such as the variations in the Nb and Ta contents and the Nb/Ta ratio in the melt [62]. Niobium contents (and Nb/Ta ratios) progressively increase in the fractionation sequence from zinnwaldite granite through muscovite–zinnwaldite granite to amazonite-bearing granite (Figure 7h). In contrast to various rare-metal granites worldwide, Shihuiyai granite—similar to Suzhou granite, Lingshan granite and Arabian Shield pegmatite—experiences an increase in Nb/Ta during fractional crystallization [63–65]. Some authors have demonstrated that a large part of the Nb may be present in micas [66], and the fractional crystallization of micas influences Nb/Ta ratios in granitic melts. The Nb content was highest in the micas of Shihuiyai zinnwaldite granite, indicating that niobium and tantalum are mainly present in mica at an early stage, and no mineral phase is formed. Niobium and tantalum in mica decrease in the amazonite-bearing granite (Figure 6d,e), indicating that the Nb-Ta-bearing melt began to precipitate niobium and tantalum oxide mineral phases, which created Nb and Ta, causing an increase in the Nb/Ta ratio in the most evolved melts. Columbite occurs as subhedral crystals in the amazonite-bearing granite and they have the same crystallization age (146.3 ± 1.1 Ma) as the granites [16], implying the precipitation of Nb-Ta oxide minerals from the highly fractionated granitic magma.

We therefore infer that fractional crystallization has played a major role in the formation of Shihuiyao granites, with amazonite-bearing granite and amazonite–pegmatite being more highly evolved with higher rare-metal content than the zinnwaldite granite and muscovite–zinnwaldite granite.

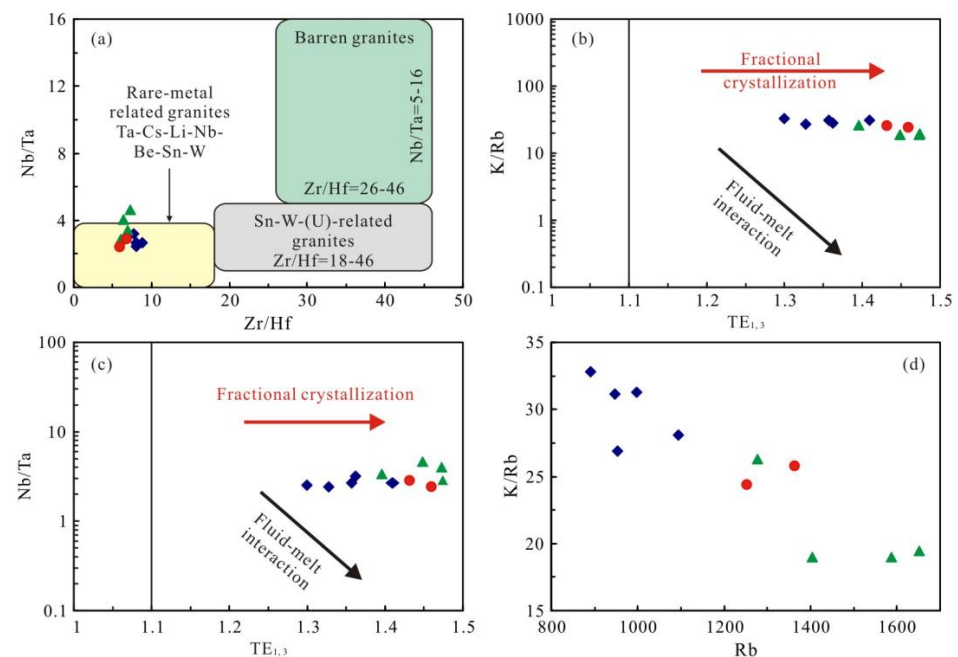


Figure 7. Cont.

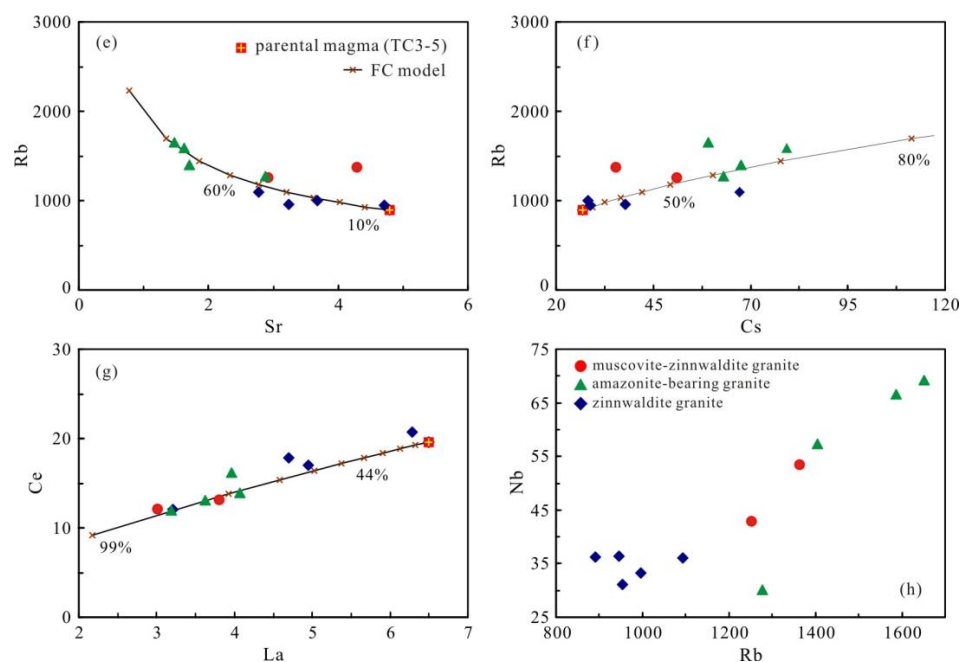


Figure 7. Diagrams of (a) Nb/Ta vs. Zr/Hf, (b) K/Rb vs. $TE_{1,3}$, (c) Nb/Ta vs. $TE_{1,3}$ and (d) K/Rb vs. Rb of the Shihuiyao samples. (e–h) Rb–Sr, Rb–Cs, La–Ce and Rb–Nb variation diagrams. The discrimination fields of (a) are based on Ballouard et al. [62]. The trendlines in (b,c) are adopted from Xue et al. [52]. For modeling Rayleigh fractionation, distribution coefficients of Rb, Sr, Cs, La and Ce in K-feldspar, plagioclase, biotite, quartz and monazite are listed in Table S1, which are taken from [67–73].

7. Conclusions

Late Jurassic Shihuiyao granites are peraluminous, low-phosphorous (PLP) rare-metal granites that follow a magmatic evolutionary trend from zinnwaldite and muscovite–zinnwaldite granite to amazonite-bearing granite. Rb is mainly hosted by micas and, to a minor degree, amazonite. These rocks contain varying amounts of manganocolumbite hosting niobium and tantalum. Extreme magmatic fractionation might be the main mechanism for Rb–Nb–Ta enrichment.

Supplementary Materials: The following supporting information can be downloaded at: <https://www.mdpi.com/article/10.3390/min13050701/s1>, Table S1: Partition coefficients used for modeling Rayleigh fractionation.

Author Contributions: Conceptualization, D.S., S.W. and J.G.; Field investigation, D.S., D.Z., J.G. and L.T.; Experimental analysis, S.W., C.D. and D.Y.; Software, J.G.; Validation, D.S., D.Z. and J.G.; Resources, D.S. and J.G.; Data Curation, D.S.; Writing—Original Draft Preparation, D.S., S.W. and J.G.; Writing—Review and Editing, D.S. and J.G.; Visualization, J.G.; Funding Acquisition, D.S. and J.G. All authors have read and agreed to the published version of the manuscript.

Funding: This work was supported by the China National Uranium Co., Ltd. and the No. 243 Team of China Nuclear Industry (Grant No. 202003), the State Key Laboratory of Ore Deposit Geochemistry open project foundation (Grant No. 201903) and Fundamental Science on Radioactive Geology and Exploration Technology Laboratory, East China University of Technology (Grant No. 2020RGET02).

Data Availability Statement: The data presented in this study are available within the article.

Acknowledgments: We greatly appreciate the thoughtful comments and very detailed, specific suggestions provided by the reviewers which have helped us to improve the quality of our manuscript. We are really grateful for the expert comments and excellent suggestions we have received.

Conflicts of Interest: The authors declare no conflict of interest.

References

1. Liao, Y.; Zhao, B.; Zhang, D.; Danyushevsky, L.V.; Li, T.; Wu, M.; Liu, F. Evidence for temporal relationship between the late Mesozoic multistage Qianlishan granite complex and the Shizhuyuan W–Sn–Mo–Bi deposit, SE China. *Sci. Rep.* **2021**, *11*, 5828. [[CrossRef](#)] [[PubMed](#)]
2. Cheng, Y.; Xu, Z.; Di, H.; Zhang, Z.; Mao, C.; Tan, H.; Huang, J.; Zhou, F.; Zhang, L.; Chen, J.; et al. Apatite U–Pb Dating and Composition Constraints for Magmatic–Hydrothermal Evolution in the Giant Renli Nb–Ta Deposit, South China. *Minerals* **2022**, *12*, 344. [[CrossRef](#)]
3. Li, P.; Li, J.; Liu, X.; Li, C.; Huang, Z.; Zhou, F. Geochronology and source of the rare-metal pegmatite in the Mufushan area of the Jiangnan orogenic belt: A case study of the giant Renli Nb–Ta deposit in Hunan, China. *Ore Geol. Rev.* **2020**, *116*, 103237. [[CrossRef](#)]
4. Yuan, S.; Mao, J.; Cook, N.J.; Wang, X.; Liu, X.; Yuan, Y. A Late Cretaceous tin metallogenic event in Nanling W–Sn metallogenic province: Constraints from U–Pb, Ar–Ar geochronology at the Jiapingling Sn–Be–F deposit, Hunan, China. *Ore Geol. Rev.* **2015**, *65*, 283–293. [[CrossRef](#)]
5. Lu, L.; Liang, T.; Chen, Z. Mineralogical Characteristics and Significance of Wolframite from the Xihuashan Tungsten Deposit, Jiangxi Province, China. *Acta Geol. Sin.* **2014**, *88*, 1470–1472. [[CrossRef](#)]
6. Li, S.; Li, J.; Chou, I.-M.; Jiang, L.; Ding, X. The formation of the Yichun Ta–Nb deposit, South China, through fractional crystallization of magma indicated by fluid and silicate melt inclusions. *J. Asian Earth Sci.* **2017**, *137*, 180–193. [[CrossRef](#)]
7. Li, X.F.; Wei, X.L.; Zhu, Y.T.; Li, Z.F.; Deng, X.C. Rare metal deposits in South China: Types, characteristics, distribution and tectonic setting. *Acta Petrol. Sin.* **2021**, *37*, 3591–3614. (In Chinese with English abstract)
8. Yang, F.; Sun, J.; Wang, Y.; Fu, J.; Na, F.; Fan, Z.; Hu, Z. Geology, Geochronology and Geochemistry of Weilasituo Sn–Polymetallic Deposit in Inner Mongolia, China. *Minerals* **2019**, *9*, 104. [[CrossRef](#)]
9. Gao, X.; Zhou, Z.; Breiter, K.; Ouyang, H.; Liu, J. Ore-formation mechanism of the Weilasituo tin–polymetallic deposit, NE China: Constraints from bulk-rock and mica chemistry, He–Ar isotopes, and Re–Os dating. *Ore Geol. Rev.* **2019**, *109*, 163–183. [[CrossRef](#)]
10. Shi, R.; Zhao, J.; Evans, N.J.; Qin, K.; Wang, F.; Li, Z.; Han, R.; Li, X. Temporal-spatial variations in Li–Fe mica compositions from the Weilasituo Sn–polymetallic deposit (NE China): Implications for deposit-scale fluid evolution. *Ore Geol. Rev.* **2021**, *134*, 104132. [[CrossRef](#)]
11. Zhu, K.-Y.; Jiang, S.-Y.; Su, H.-M.; Duan, Z.-P. In situ geochemical analysis of multiple generations of sphalerite from the Weilasituo Sn–Li–Rb–Cu–Zn ore field (Inner Mongolia, northeastern China): Implication for critical metal enrichment and ore-forming process. *Ore Geol. Rev.* **2021**, *139*, 104473. [[CrossRef](#)]
12. Zhang, L.; Jiang, S.-Y. Two episodic Nb–Ta mineralization events and genesis of the Zhaojinggou rare-metal deposit, north margin of the North China Craton. *Ore Geol. Rev.* **2021**, *131*, 103994. [[CrossRef](#)]
13. Wu, C.Z.; Jia, L.; Lei, R.X.; Chen, B.Y.; Feng, Z.J.; Feng, Y.G.; Zhi, J.; Bai, S.H. Advances and general characteristics of the amazonite granite and related rubidium deposits in Central Asian Orogenic Belt. *Acta Petrol. Sin.* **2021**, *37*, 2604–2628. (In Chinese with English Abstract)
14. Duan, Z.P.; Jiang, S.Y.; Su, H.M.; Zhu, X.Y.; Zou, T.; Cheng, X.Y. Trace and Rare Earth Elements, and Sr Isotopic Compositions of Fluorite from the Shihuiyao Rare Metal Deposit, Inner Mongolia: Implication for Its Origin. *Minerals* **2020**, *10*, 882. [[CrossRef](#)]
15. Zhu, J.Z.; Lu, X.C.; Yao, Z.W. Geological characteristics and metallogenic regularity of rare metal desposit in Shihuiyao, Inner Mongolia. *Miner. Explor.* **2013**, *4*, 635–641. (In Chinese with English Abstract)
16. Zhou, Z.; Breiter, K.; Wilde, S.A.; Gao, X.; Burnham, A.D.; Ma, X.; Zhao, J. Ta–Nb mineralization in the shallow-level highly-evolved P-poor Shihuiyao granite, Northeast China. *Lithos* **2022**, *416–417*, 106655. [[CrossRef](#)]
17. Zhang, T.; Hou, Z.; Pan, X.; Duan, L.; Xiang, Z. Cassiterite geochemistry and U–Pb geochronology of the Shihuiyao Rb–(Nb–Ta–Be–Sn) deposit, Northeast China: Implication for ore-forming processes and mineral exploration. *Ore Geol. Rev.* **2023**, *156*, 105393. [[CrossRef](#)]
18. Duan, Z.-P.; Jiang, S.-Y.; Su, H.-M.; Zhu, X.-Y.; Zou, T.; Cheng, X.-Y. Geochronological and geochemical investigations of the granites from the giant Shihuiyao Rb–(Nb–Ta–Be–Li) deposit, Inner Mongolia: Implications for magma source, magmatic evolution, and rare metal mineralization. *Lithos* **2021**, *400–401*, 106415. [[CrossRef](#)]
19. Han, J.T.; Yuan, T.M.; Liu, W.Y.; Liu, L.J.; Liu, G.X.; Hou, H.S.; Wang, T.Q.; Guo, Z.Y.; Kang, J.Q.; Zhang, J.H. Geoelectric structure of the collision zone between the Siberia plate and the North China Craton and discussion on the deep suture boundary. *Chin. J. Geophys.* **2019**, *62*, 1159–1171, (In Chinese with English Abstract).
20. Ge, M.; Zhou, W.; Yu, Y.; Sun, J.; Bao, J.; Wang, S. Dissolution and supracrustal rocks dating of Xilin Gol Complex, Inner Mongolia, China. *Earth Sci. Front.* **2011**, *18*, 182–1951. (In Chinese with English Abstract)
21. Xu, W.L.; Pei, F.P.; Wang, F.; Meng, E.; Ji, W.Q.; Yang, D.B.; Wang, W. Spatial–Temporal relationships of Mesozoic volcanic rocks in NE China: Constraints on tectonic overprinting and transformations between multiple tectonic systems. *J. Asian Earth Sci.* **2013**, *74*, 167–193. [[CrossRef](#)]
22. Ouyang, H.G.; Mao, J.W.; Santosh, M.; Zhou, J.; Zhou, Z.H.; Wu, Y.; Hou, L. Geodynamic setting of Mesozoic magmatism in NE China and surrounding regions: Perspectives from spatio-temporal distribution patterns of ore deposits. *J. Asian Earth Sci.* **2013**, *78*, 222–236. [[CrossRef](#)]
23. Deng, C.; Sun, D.; Li, G.; Lu, S.; Tang, Z.; Gou, J.; Yang, Y. Early Cretaceous volcanic rocks in the Great Xing’an Range: Late effect of a flat-slab subduction. *J. Geodyn.* **2019**, *124*, 38–51. [[CrossRef](#)]

24. Deng, C.; Sun, D.; Ping, X.; Huang, H.; Zhang, L.; Lu, S. Geochemistry of Early Cretaceous volcanic rocks in the Northeastern Great Xing'an Range, northeast China and implication for geodynamic setting. *Int. Geol. Rev.* **2019**, *61*, 1594–1612. [[CrossRef](#)]
25. Tian, L.; Sun, D.; Gou, J.; Jiang, S.; Feng, Z.; Zhang, D.; Hao, Y. Petrogenesis of the Newly Discovered Early Cretaceous Peralkaline Granitic Dikes in Baerzhe Area of Jarud Banner, Inner Mongolia: Implications for Deciphering Magma Evolution. *Minerals* **2022**, *12*, 1532. [[CrossRef](#)]
26. Tang, Z.-Y.; Sun, D.-Y.; Mao, A.-Q.; Yang, D.-G.; Deng, C.-Z. Timing and evolution of Mesozoic volcanism in the central Great Xing'an Range, northeastern China. *Geol. J.* **2019**, *54*, 3737–3754. [[CrossRef](#)]
27. Yang, J.-H.; Chen, H.; Zhou, M.-F.; Hu, R.-Z.; Williams-Jones, A.E. Lithium isotope fractionation during intensive felsic magmatic differentiation. *Geochem. Geophys. Geosyst.* **2023**, *24*, e2022GC010771. [[CrossRef](#)]
28. Wang, X.; Chen, X.; Zou, J.Z.; Li, B.; Wang, H.; Xu, D. Geochronology, geochemistry, and mineral chemistry of the Lingshan-Huangshan complex, South China: Insights into Nb and Ta enrichment. *Ore Geol. Rev.* **2023**, *157*, 105433. [[CrossRef](#)]
29. Liu, Y.S.; Hu, Z.C.; Gao, S.; Günther, D.; Xu, J.; Gao, C.G.; Chen, H.H. In situ analysis of major and trace elements of anhydrous minerals by LA-ICP-MS without applying an internal standard. *Chem. Geol.* **2008**, *257*, 34–43. [[CrossRef](#)]
30. Tang, Y.; Wang, H.; Zhang, H.; Lv, Z.-H. K-feldspar composition as an exploration tool for pegmatite-type rare metal deposits in Altay, NW China. *J. Geochem. Explor.* **2018**, *185*, 130–138. [[CrossRef](#)]
31. Linnen, R.L.; Cuney, M. Granite-related rare-element deposits and experimental constraints on Ta-Nb-W-Sn-Zr-Hf mineralization. In *Rare-Element Geochemistry and Mineral Deposits*; Linnen, R.L., Samson, I.M., Eds.; Geological Association of Canada Short Course Notes; Mineralogical Association of Canada: Ottawa, ON, Canada, 2005; Volume 17, pp. 45–67.
32. Chappell, B.W.; White, A.J.R. Two contrasting granite types. *Pac. Geol.* **1974**, *8*, 173–174.
33. Peccerillo, A.; Taylor, S.R. Geochemistry of Eocene calc-alkaline volcanic rocks from the Kastamonu area, Northern Turkey. *Contrib. Mineral. Petrol.* **1976**, *58*, 63–81. [[CrossRef](#)]
34. Blevin, P. Metallogeny of granitic rocks, The Ishihara Symposium. *Granites Assoc. Metallog.* **2003**, *14*, 5–8.
35. Boynton, W.V. Cosmochemistry of the Rare Earth Elements: Meteorite Studies. *Dev. Geochem.* **1984**, *2*, 63–114.
36. Sun, S.S.; McDonough, W.F. Chemical and isotopic systematics of oceanic basalts: Implications for mantle composition and processes. *Geol. Soc. Lond. Spec. Publ.* **1989**, *42*, 313–345. [[CrossRef](#)]
37. Watson, E.B.; Harrison, T.M. Zircon saturation revisited: Temperature and composition effects in a variety of crustal magma types. *Earth Planet. Sci. Lett.* **1983**, *64*, 295–304. [[CrossRef](#)]
38. Cuney, M. Felsic magmatism and uranium deposits. *Bull. De La Société Géologique De Fr.* **2014**, *185*, 75–92. [[CrossRef](#)]
39. Eby, G.N. Chemical subdivision of the A-type granitoids: Petrogenetic and tectonic implications. *Geology* **1992**, *20*, 641–644. [[CrossRef](#)]
40. White, A.J.R.; Chappell, B.W. Granitoid types and their distribution in the Lachlan Fold Belt, southeastern Australia. *Geol. Soc. Am.* **1983**, *159*, 21–34.
41. Zhao, Z.H.; Xiong, X.L.; Hen, X.D.; Wang, Y.X.; Qiang, W.; Bao, Z.W.; Jahn, B. Controls on the REE tetrad effect in granites: Evidence from the Qianlishan and Baerzhe granites, China. *Geochem. J.* **2002**, *36*, 527–543.
42. Wu, F.Y.; Liu, X.C.; Ji, W.Q.; Wang, J.M.; Yang, L. Highly fractionated granites: Recognition and research. *Sci. China Earth Sci.* **2017**, *60*, 1201–1219. [[CrossRef](#)]
43. Wang, Z.; Zhao, X.; Yu, S.; Li, S.; Peng, Y.; Liu, Y. Cretaceous granitic intrusions in Fujian Province, Cathaysia Block: Implications for slab rollback and break-off of the Paleo-Pacific plate. *J. Asian Earth Sci.* **2020**, *190*, 104164. [[CrossRef](#)]
44. Li, J.W.; Zhao, X.F.; Zhou, M.F.; Ma, C.Q.; de Souza, Z.S.; Vasconcelos, P. Late Mesozoic magmatism from the Daye region, eastern China: U–Pb ages, petrogenesis, and geodynamic implications. *Contrib. Mineral. Petrol.* **2009**, *157*, 383–409. [[CrossRef](#)]
45. Li, X.H.; Li, Z.X.; Li, W.X.; Liu, Y.; Yuan, C.; Wei, G.J.; Qi, C.S. U–Pb zircon, geochemical and Sr–Nd–Hf isotopic constraints on age and origin of Jurassic I- and A-type granites from central Guangdong, SE China: A major igneous event in response to foundering of a subducted flat-slab? *Lithos* **2007**, *96*, 186–204. [[CrossRef](#)]
46. Chappell, B.W.; White, A.J.R. I- and S-type granites in the Lachlan Fold Belt. *Earth Environ. Sci. Trans. R. Soc. Edinb.* **1992**, *83*, 1–26.
47. Patino Douce, A.E. What do experiments tell us about the relative contributions of crust and mantle to the origin of granitic magmas? *Geol. Soc. Lond. Spec. Publ.* **1999**, *168*, 55–75. [[CrossRef](#)]
48. Wedepohl, K.H. The composition of the continental crust. *Geochim. Et Cosmochim. Acta* **1995**, *59*, 1217–1232. [[CrossRef](#)]
49. Rudnick, R.L.; Gao, S. Composition of the continental crust. *Treatise Geochem.* **2003**, *3*, 1–64.
50. Plank, T. Constraints from thorium/lanthanum on sediment recycling at subduction zones and the evolution of the continents. *J. Petrol.* **2005**, *46*, 921–944. [[CrossRef](#)]
51. Peretyazhko, I.S.; Savina, E.A. Tetrad effects in the rare earth element patterns of granitoid rocks as an indicator of fluoride-silicate liquid immiscibility in magmatic systems. *Petrology* **2010**, *18*, 514–543. [[CrossRef](#)]
52. Xue, S.; Li, S.-M.; Zhu, D.-C.; Wang, Q.; Zhang, L.-L.; Zhao, Z. Tetrad effect of rare earth elements caused by fractional crystallization in high-silica granites: An example from central Tibet. *Lithos* **2021**, *384–385*, 105968.
53. Zozulya, D.; Macdonald, R.; Bagiński, B.; Jokubauskas, P. Nb/Ta, Zr/Hf and REE fractionation in exotic pegmatite from the Keivy province, NW Russia, with implications for rare-metal mineralization in alkali feldspar granite systems. *Ore Geol. Rev.* **2022**, *143*, 104779. [[CrossRef](#)]

54. Martins, I.; Mateus, A.; Cathelineau, M.; Boiron, M.C.; da Costa, I.R.; da Silva, D.; Gaspar, M. The Lanthanide “Tetrad Effect” as an Exploration Tool for Granite-Related Rare Metal Ore Systems: Examples from the Iberian Variscan Belt. *Minerals* **2022**, *12*, 1067. [[CrossRef](#)]
55. Zeng, L.S.; Gao, L.E. Cenozoic crustal anatexis and the leucogranites in the Himalayan collisional orogenic belt. *Acta Petrol. Sin.* **2017**, *33*, 1420–1444. (In Chinese with English Abstract)
56. Zeng, L.S.; Asimow, P.D.; Saleeby, J.B. Coupling of anatectic reactions and dissolution of accessory phases and the Sr and Nd isotope systematics of anatectic melts from a metasedimentary source. *Geochim. Et Cosmochim. Acta* **2005**, *69*, 3671–3682. [[CrossRef](#)]
57. Roda-Robles, E.; Keller, P.; Pesquera, A.; Fontan, F. Micas of the muscovite–lepidolite series from Karibib pegmatites, Namibia. *Mineral. Mag.* **2007**, *71*, 41–62. [[CrossRef](#)]
58. Linnen, R.L. The solubility of Nb–Ta–Zr–Hf–W in granitic melts with Li and Li + F: Constraints for mineralization in rare metal granites and pegmatites. *Econ. Geol.* **1998**, *93*, 1013–1025. [[CrossRef](#)]
59. Alferyeva, Y.O.; Chevychelov, V.Y.; Novikova, A.S. Experimental Study of the Crystallization Conditions of Ongonites of the Ary-Bulak Massif (Eastern Transbaikalia). *Petrology* **2022**, *30*, 212–225. [[CrossRef](#)]
60. Manning, D.A.C. The Effect of Fluorine on Liquidus Phase Relationships in the System Qz-Ab-Or with Excess Water at 1 kb. *Contrib. Mineral. Petrol.* **1981**, *76*, 206–215. [[CrossRef](#)]
61. Bailey, J.C. Fluorine in granitic rocks and melts: A review. *Chem. Geol.* **1977**, *19*, 1–42. [[CrossRef](#)]
62. Ballouard, C.; Poujol, M.; Boulvais, P.; Branquet, Y.; Tartèse, R.; Vigneresse, J.-L. Nb-Ta fractionation in peraluminous granites: A marker of the magmatic hydrothermal transition. *Geology* **2016**, *44*, 231–234. [[CrossRef](#)]
63. He, S.; Li, Z.; Jehani, A.A.; Guo, D.; Harbi, Z.; Zhang, Y. Nb–Ta Behaviour during Magma-to-Pegmatite Transformation Process: Record from Zircon Megacrysts in Pegmatite. *Minerals* **2021**, *11*, 1139. [[CrossRef](#)]
64. Tian, E.; Xie, L.; Wang, R.; Duan, X.; Huang, F.; Che, X.; Chen, X.; Wang, L. Mineralogical constraints on Nb-Ta fractionation in Early Cretaceous A-type granites from the Suzhou pluton, SE China. *Lithos* **2021**, *402–403*, 106286. [[CrossRef](#)]
65. Xiang, Y.X.; Yang, J.H.; Chen, J.Y.; Zhang, Y. Petrogenesis of Lingshan highly fractionated granites in the Southeast China: Implication for Nb-Ta mineralization. *Ore Geol. Rev.* **2017**, *89*, 497–525. [[CrossRef](#)]
66. Zhu, Z.; Wang, R.; Marignac, C.; Cuney, M.; Mercadier, J.; Che, X.; Lespinasse, M.-Y. A new style of rare metal granite with Nb-rich mica: The Early Cretaceous Huangshan rare-metal granite suite, northeast Jiangxi Province, southeast China. *Am. Mineral.* **2018**, *103*, 1530–1544. [[CrossRef](#)]
67. Irber, W. The Lanthanide Tetrad Effect and its Correlation with K/Rb, Eu/Eu*, Sr/Eu, Y/Ho and Zr/Hf of Evolving Peraluminous Granite Suits. *Geochim. Et Cosmochim. Acta* **1999**, *63*, 489–508. [[CrossRef](#)]
68. Nash, W.P.; Crecraft, H.R. Partition coefficients for trace elements in silicic magmas. *Geochim. Et Cosmochim. Acta* **1986**, *49*, 2309–2322. [[CrossRef](#)]
69. Long, P.E. Experiment determination of partition coefficients for Rb, Sr and Ba between alkali feldspar and silicate liquid. *Geochim. Et Cosmochim. Acta* **1978**, *42*, 833–846. [[CrossRef](#)]
70. Stix, J.; Gorton, M.P. Variations in trace element partition coefficients in sanidine in the Cerro Toledo Rhyolite, Jemez Mountains, New Mexico: Effects of composition, temperature, and volatiles. *Geochim. Et Cosmochim. Acta* **1990**, *54*, 2697–2708. [[CrossRef](#)]
71. Fujimaki, H.; Tatsumoto, M.; Aoki, K. Partition coefficients of Hf, Zr and REE between phenocrysts and groundmasses. *J. Geophys. Res.* **1984**, *89*, B662–B672. [[CrossRef](#)]
72. Were, P.; Keppler, H. Trace element fractionation between biotite, allanite, and granitic melt. *Contrib. Mineral. Petrol.* **2021**, *176*, 74. [[CrossRef](#)]
73. Stepanov, A.S.; Hermann, J.; Rubatto, D.; Rapp, R.P. Experimental study of monazite/melt partitioning with implications for the REE, Th and U geochemistry of crustal rocks. *Chem. Geol.* **2012**, *300–301*, 200–220. [[CrossRef](#)]

Disclaimer/Publisher’s Note: The statements, opinions and data contained in all publications are solely those of the individual author(s) and contributor(s) and not of MDPI and/or the editor(s). MDPI and/or the editor(s) disclaim responsibility for any injury to people or property resulting from any ideas, methods, instructions or products referred to in the content.